



HAL
open science

Three-dimensional displacement field of the 2015 Mw8.3 Illapel earthquake (Chile) from across- and along-track Sentinel-1 TOPS interferometry

Raphael Grandin, Emilie Klein, Marianne Métois, Christophe Vigny

► To cite this version:

Raphael Grandin, Emilie Klein, Marianne Métois, Christophe Vigny. Three-dimensional displacement field of the 2015 Mw8.3 Illapel earthquake (Chile) from across- and along-track Sentinel-1 TOPS interferometry. *Geophysical Research Letters*, 2016, 10.1002/2016GL067954 . hal-01320480v1

HAL Id: hal-01320480

<https://hal.science/hal-01320480v1>

Submitted on 23 May 2016 (v1), last revised 23 Oct 2017 (v2)

HAL is a multi-disciplinary open access archive for the deposit and dissemination of scientific research documents, whether they are published or not. The documents may come from teaching and research institutions in France or abroad, or from public or private research centers.

L'archive ouverte pluridisciplinaire **HAL**, est destinée au dépôt et à la diffusion de documents scientifiques de niveau recherche, publiés ou non, émanant des établissements d'enseignement et de recherche français ou étrangers, des laboratoires publics ou privés.

1 3D displacement field of the 2015 M_w 8.3 Illapel 2 earthquake (Chile) from across- and along-track 3 Sentinel-1 TOPS interferometry

R. Grandin¹, E. Klein², M. Métois³, and C. Vigny²

Abstract

4 Wide-swath imaging has become a standard acquisition mode for radar missions aiming at
5 applying SAR interferometry at global scale with enhanced revisit frequency. Increased swath
6 width, compared to classical Stripmap imaging mode, is achieved at the expense of azimuthal
7 resolution. This makes along-track displacements, and subsequently north-south displacements,
8 difficult to measure using conventional split-beam (multiple-aperture) InSAR or cross-correlation
9 techniques. Alternatively, we show here that the along-track component of ground motion can
10 be deduced from the double-difference between backward- and forward-looking interferograms
11 within regions of burst overlap. “Burst overlap interferometry” takes advantage of the large
12 squint angle diversity of Sentinel-1 ($\sim 1^\circ$) to achieve sub-decimeter accuracy on the along-track
13 component of ground motion. We demonstrate the efficiency of this method using Sentinel-1 data
14 covering the 2015 M_w 8.3 Illapel earthquake (Chile) for which we retrieve the full 3D displacement
15 field and validate it against observations from a dense network of GPS sensors.

1. Introduction

16 Since the pioneering contributions of the 1990s, monitoring of large-scale ground motion
17 using Interferometric Synthetic Aperture Radar (InSAR) has made spectacular progress.
18 Thanks to improvement of the phased array technology, advances in orbitography, in-
19 creasing computational power as well as the launch of multiple civilian SAR missions
20 since the 2000s, a broad range of natural and anthropogenic processes can be routinely
21 monitored today [see *Simons and Rosen*, 2007, for a recent review]. Among these pro-
22 cesses, the InSAR technique has proved extremely valuable in mapping the displacement

¹Institut de Physique du Globe de Paris,
Sorbonne Paris Cité, Université Paris
Diderot, UMR 7154 CNRS, Paris, France.

²Laboratoire de Géologie, École Normale
Supérieure, UMR 8538 CNRS, Paris,
France.

³Laboratoire de Géologie de Lyon: Terre,
Planètes, Environnement (LGLTPE), École
Normale Supérieure de Lyon, Université
Claude Bernard, UMR 5276 CNRS, Lyon,
France.

23 field induced by large plate-boundary events, such as earthquakes or magmatic intrusions,
24 especially in geographical areas where GPS measurements are lacking [e.g. *Peltzer et al.*,
25 1999; *Grandin et al.*, 2009].

26 One limitation of InSAR is that only the component of deformation in the sensor line-of-
27 sight (LOS), i.e. the across-track component, can be resolved. Acquisitions from ascending
28 and descending passes are usually combined to provide two different viewing geometries.
29 Even so, due to the near-polar orbit of SAR satellites, resolution on the north-south com-
30 ponent remains poor [*Wright et al.*, 2004].

31 Therefore, in complement to conventional InSAR, a number of signal processing tech-
32 niques have been proposed to retrieve the horizontal component of displacement parallel
33 to the satellite track. These methods, which rely either on the amplitude (incoherent
34 cross-correlation, also termed offset tracking [*Michel et al.*, 1999; *Fialko et al.*, 2001]) or
35 on the phase (multiple-aperture InSAR, also termed split-beam interferometry [*Bechor*
36 *and Zebker*, 2006; *Barbot et al.*, 2008; *Jung et al.*, 2009]), typically allow for resolving
37 displacements exceeding $\sim 10\%$ of the azimuth pixel size. Hence, for classical Stripmap
38 mode (azimuth pixel size of the order of a few meters), displacements greater than a few
39 decimeters can be resolved. As a consequence, the resolution that can be achieved with
40 such methods restricts their applicability to the study of intermediate to large earthquakes
41 ($M_w > 6$).

42 Recent advances in SAR technology and processing have allowed for the emergence of a
43 new generation of sensors entirely dedicated to wide-swath imaging. Wide-swath modes
44 allow for global mapping with an increased revisit frequency, as exemplified by the two

45 satellites Sentinel-1 and ALOS-2, respectively operating TOPS and ScanSAR as stan-
46 dard acquisition modes. Unfortunately, the increase of the swath breadth by a factor
47 3 to 5 comes at the expense of reduced azimuthal resolution by an equivalent factor.
48 Trading azimuth resolution for increased swath width, hence shortened revisit interval, is
49 arguably advantageous for studying large-scale tectonic deformation, whether coseismic,
50 postseismic or interseismic [e.g. *Grandin et al.*, 2015]. On the other hand, split-beam and
51 offset-tracking techniques become limited to sensing along-track displacement exceeding
52 ~ 50 cm, hence restricting their potential usefulness [*Jung et al.*, 2014].

53 Alternatively, we propose here to take advantage of wide-swath burst-modes, especially
54 TOPS, by applying along-track interferometry in regions where successive bursts over-
55 lap in the azimuth direction (Figure 1). This technique, whose original objective was
56 to improve the coregistration of a slave image against its master [*Scheiber and Moreira*,
57 2000; *Prats-Iraola et al.*, 2012], is used here for another purpose. We show that burst-
58 overlap interferometry allows for resolving subtle motion along the azimuth direction. The
59 technique is particularly efficient for Sentinel-1 TOPS data, as beam steering in azimuth
60 provides an increased squint angle diversity within burst overlaps, hence a better resolu-
61 tion on horizontal motion compared to split-beam interferometry applied to Stripmap or
62 ScanSAR images.

63 In this paper, focusing on the case study of the Illapel earthquake (Chile, 16 September
64 2015, $M_w 8.3$), we use Sentinel-1 wide-swath data to retrieve the full 3D surface displace-
65 ment field. Independent measurements acquired by a continuous GPS network allow for
66 validating the method and estimating its uncertainty.

2. Method

2.1. TOPS along-track interferometry

67 Sentinel-1 is the first SAR mission to implement the TOPS mode as a standard acqui-
68 sition mode for interferometry (Figure 1) [*Torres et al.*, 2012]. Similar to ScanSAR, an
69 extended swath is achieved in TOPS mode by electronically steering the beam in eleva-
70 tion periodically so as to cover several adjacent sub-swaths (three in the case of Sentinel-1
71 “Interferometric Wide-swath” mode, IW) [*De Zan and Guarnieri*, 2006]. Each sub-swath
72 is imaged in a succession of bursts, typically consisting of a thousand pulses. Because a
73 given ground pixel is only illuminated during a fraction of the standard Stripmap-mode
74 synthetic aperture duration, the resulting azimuth bandwidth of burst-modes, hence the
75 achievable azimuth resolution, is decreased accordingly. On the other hand, the range
76 properties of the images (bandwidth and resolution) are unchanged.

77 In ScanSAR mode, the beam angle with respect to zero-Doppler direction (also termed
78 “squint” angle) is held fixed. In TOPS mode, a steady drift of the squint angle, from
79 backward to forward, is introduced over the course of the burst transmission in order
80 to broaden the size of the illuminated area in the azimuth direction (Figure 1a). As a
81 result, TOPS achieves improved image quality both in terms of phase (reduced azimuth
82 ambiguity) and amplitude (decreased “scalloping” effect) [*Meta et al.*, 2008]. Nevertheless,
83 both ScanSAR and TOPS require accurate burst synchronization to warrant sufficient
84 azimuth spectral overlap for interferometry [*Holzner and Bamler*, 2002].

85 In wide-swath mode, a small overlap region occurs between the bursts to ensure that
86 the final processed image will be devoid of any gap (Figure 1a). In these “burst overlap
87 regions”, ground pixels are observed twice from two slightly different angles, or equiva-

88 lently with two different Doppler centroid frequencies (Figure 1b). In ScanSAR mode, this
 89 azimuth angular separation is limited by beam aperture, which usually does not exceed
 90 0.25° . In TOPS mode, the Doppler centroid difference is much greater, as a direct conse-
 91 quence of the squinted view introduced by beam steering in azimuth. For Sentinel-1, the
 92 difference in squint angle is typically of the order of 1° , with overlap regions corresponding
 93 to $\sim 10\%$ of the burst length.

94 When processing TOPS data for interferometry, it is possible to take advantage of the
 95 slight difference in squint angles within overlap regions in order to retrieve the horizontal
 96 component of ground motion parallel to the satellite track. Akin to Multiple Aperture
 97 InSAR (MAI), a double difference of the phase within overlap regions is computed as
 98 follows (Figure 1b) : (1) calculate the interferogram using only the phase deduced from
 99 the forward view $\Delta\Phi_{\text{fw}}$, (2) calculate the interferogram in the backward view $\Delta\Phi_{\text{bw}}$,
 100 (3) compute the difference between forward-looking and backward-looking interferograms
 101 $\Delta\Phi_{\text{ovl}} = \Delta\Phi_{\text{fw}} - \Delta\Phi_{\text{bw}}$ (see Appendix A for details). This technique will be thereafter
 102 referred to as “burst-overlap interferometry”.

103 The final double-difference interferogram corresponds to the temporal variation of the
 104 difference in slant range from two slightly different squint angles. In observation scenarios
 105 devoid of any ground motion, the double-difference phase $\Delta\Phi_{\text{ovl}}$ only includes the effect
 106 of slight errors in coregistration between the master and slave images [*Scheiber and Mor-*
 107 *eira, 2000*]. Hence, this procedure is commonly used to refine coregistration during TOPS
 108 InSAR processing, a method known as “enhanced spectral diversity” (ESD) [e.g. *Prats-*
 109 *Iraola et al., 2012*]. On the other hand, when significant ground motion has occurred

110 between two acquisitions, phase jumps across burst boundaries in TOPS interferograms
111 are diagnostic of horizontal ground motion along the satellite track [e.g. *De Zan et al.*,
112 2014; *González et al.*, 2015]. The double-difference procedure allows for directly measur-
113 ing this phase difference on a pixelwise basis within overlap regions. Topographic and
114 tropospheric contributions are largely cancelled by the double-difference, which results in
115 better phase quality than in the across-track interferogram.

2.2. Data set

116 In order to map the 3D displacement field of the 2015 M_w 8.3 Illapel earthquake, we
117 use SAR data acquired by Sentinel-1A in IW TOPS mode. Images before the earthquake
118 were acquired on 08/24/2015 and 08/26/2015 for the descending and ascending passes,
119 respectively. Post-earthquakes acquisitions were performed on 09/17/2015 (+11 hours
120 after quake) and 09/19/2015 (+3 days). Interferograms are computed using the method
121 of *Grandin* [2015], starting from Level 1 Single Look Complex (SLC) products distributed
122 by ESA. Precise orbits (<https://qc.sentinel1.eo.esa.int>) and SRTM 1-arcsecond DEM are
123 used for orbital and topographic corrections. Azimuth phase deramping is calculated
124 using precise coregistration derived from pixel offsets, and further refined by means of
125 ESD within burst overlaps [*Prats-Iraola et al.*, 2012; *Grandin*, 2015]. Interferograms are
126 multilooked by a factor 12 in range and 4 in azimuth, resulting in a ground pixel of
127 ~ 60 m. Unwrapping is performed using the cut-tree algorithm [*Goldstein et al.*, 1988]
128 and corrected manually when necessary.

129 Azimuth displacements are retrieved using the burst overlap interferometry technique
130 (see Appendix A for details). Flat-Earth, topographic correction and multilooking are

131 applied to the forward and backward interferograms prior to computation of the double-
132 difference interferogram [De Zan *et al.*, 2015]. A spatial coherence mask with a threshold
133 of 0.4 is applied to discard unreliable phase values. Pixels are low-pass filtered using 1 km-
134 wide maximum likelihood estimator. Flattening of interferograms is performed by fitting
135 a bilinear polynomial surface on the difference between, on one hand, GPS measurements
136 from a local geodetic network [Ruiz *et al.*, 2016] projected onto the appropriate unit vector
137 (along- or across-track) and, on the other hand, the nearest pixel in the interferogram.
138 Finally, interpolation by a Laplacian operator is applied in order to fill the gaps between
139 the bursts.

3. Results and discussion

3.1. Along-track InSAR

140 Across-track interferograms show a maximum line-of-sight displacement of ± 150 cm,
141 picturing the semi-circular fringe pattern typical of subduction earthquakes in Chile [e.g.
142 Pritchard *et al.*, 2006] (Figure 2, top). Displacement occurs exclusively away from the
143 satellite in the descending pass and toward the satellite in the ascending pass. This
144 is consistent with seaward motion reaching $\gtrsim 1$ m in the coastal area combined with
145 moderate vertical displacement (within the range ± 50 cm) due to the offshore earthquake
146 location. Furthermore, we notice that peak displacement in the descending across-track
147 interferogram occurs ~ 30 km to the north of the peak in the ascending interferogram.
148 This suggests that displacement vectors experience substantial rotation, either about a
149 vertical or horizontal axis, at 31° S. However, as a result of the acquisition geometry of
150 InSAR, the vertical and north-south components cannot be distinguished in the across-

151 track interferograms. Hence, all the details of the actual ground displacement field cannot
152 be restituted solely from these two across-track interferograms.

153 In contrast, along-track interferograms show a more complex displacement pattern with
154 both negative and positive displacements peaking at ± 40 cm (Figure 2, bottom). Dis-
155 placements vary smoothly over distances exceeding ~ 20 km, which is twice the distance
156 separating two consecutive burst overlap regions. This demonstrates that interpolation
157 between burst overlaps did not lead to significant aliasing of the displacement field. Due
158 to the near-polar orbit, along-track interferograms are strongly sensitive to the north-
159 south component of motion, whereas across-track interferograms are least sensitive to
160 this component. In the particular case of the Illapel earthquake, horizontal displacement
161 occurs mostly trench-normal, i.e. with an azimuth of $N260^\circ$. The ascending along-track
162 interferogram, which is nearly insensitive to the trench-normal displacement, shows a sign
163 reversal consistent with trench-parallel, southward motion in the north, shifting to trench-
164 parallel, northward motion in the south. In the along-track descending interferogram,
165 peak displacement occurs in the northern part, at $30.7^\circ S$, which is also compatible with
166 a significant component of southward displacement in that area. These trench-parallel
167 displacements are consistent with a radial, centripetal pattern of horizontal displacement
168 vectors pointing toward the centroid of the earthquake. This effect is most pronounced
169 toward the north and south edges of the main slip area, a feature that can be used to
170 refine source models of the earthquake.

3.2. Comparison with GPS data

171 Projection of GPS displacements in the line-of-sight and along the direction of the
172 satellite track allows for validating the accuracy of the interferometric products for across-
173 track and along-track interferograms, respectively (Figure 3). This comparison yields a
174 root mean square (RMS) residual of 7.8 cm and 7.0 cm for ascending and descending
175 across-track interferograms, respectively. This residual is close to the fluctuations of 1–2
176 fringes usually observed within across-track C-band interferograms in north-central Chile
177 [Ducret, 2013]. Linear regression between across-track InSAR and GPS projected in the
178 LOS shows an excellent mutual agreement, with a coefficient of correlation above 0.98
179 and a proportionality factor within 10% of unity.

180 For the along-track component, the RMS equals 3.5 cm and 5.9 cm for ascending and
181 descending geometries, respectively. This sub-decimeteric misfit is in agreement with theo-
182 retical expectations (see Appendix A for details). The slope of the linear regression is close
183 to 0.8 in either case. This value departs from unity, which may be due to bias on the slope
184 determination imparted by misfits on the few points located in the area of maximum dis-
185 placement along the coast. In particular, maximum misfit in the descending along-track
186 interferogram chiefly occurs at site EMAT, which has recorded a peak westward displace-
187 ment of 220 cm. Due to instrument malfunction, the GPS-derived coseismic displacement
188 at EMAT includes 2 days of post-seismic displacement that are largely absent in the
189 descending interferogram (post-quake image acquired +11 hours after mainshock). Yet,
190 significant post-seismic motion, likely resulting from rapid afterslip, is evident in time-
191 series from cGPS sites located along the coast (6–7 cm eastward displacement is recorded

192 in the 24 hours following the mainshock at sites CMBA and PFRJ). Therefore, significant
193 residual post-seismic motion may explain part of the misfit at EMAT.

3.3. 3D displacement field

194 The 3D displacement field can be deduced from the four components of ground motion
195 sensed by across- and along-track interferograms on both ascending and descending geome-
196 tries (Figure 4). This is achieved by solving an overdetermined linear system involving 3
197 unknowns and 4 equations, consisting in the LOS and azimuth displacements in ascending
198 and descending passes. The agreement between GPS- and InSAR-derived displacements
199 is below 3 cm for the vertical and east-west components, which are best resolved. The
200 RMS is only slightly higher (5.3 cm) for the north-south component, which would other-
201 wise remain unresolved by standard across-track InSAR. The rotation of displacement
202 vectors along the shoreline is well reproduced, as well as the shift from coastal subsidence
203 to coastal uplift at 31.1°S. This change is consistent with vertical motion recorded by
204 intertidal fauna [Ruiz *et al.*, 2016]. Coseismic slip extending below the continent near the
205 epicenter, and remaining offshore further to the north, explains this feature [Ruiz *et al.*,
206 2016; Melgar *et al.*, 2016].

4. Conclusion

207 This study demonstrates the capability of the Sentinel-1 system, operating in wide-
208 swath TOPS mode, to capture the full 3D displacement field of large subduction earth-
209 quakes at sub-decimeter accuracy for all three components. In the particular case of
210 an earthquake where horizontal displacement is predominantly east-west, and displace-
211 ments vary smoothly, such as large subduction earthquakes in South America, Japan or

212 Cascadia, Sentinel-1 allows for quickly and exhaustively mapping surface displacement.
 213 For shallower and/or smaller earthquakes, the method may partly miss the variability
 214 of the displacement over length scales smaller than 10 km, as along-track interferometry
 215 is only practicable in burst overlap regions. Nevertheless, within burst overlap regions,
 216 the along-track component of displacement is available at dense spatial sampling, and is
 217 not influenced by tropospheric phase screen. This is similar to having a densely-spaced
 218 campaign GPS transect at disposal, which already represents a substantial improvement.
 219 Between these sparse burst overlap regions, conventional split-beam and/or offset-tracking
 220 can provide a background measurement, albeit with less accuracy [*Jung et al.*, 2014;
 221 *Scheiber et al.*, 2015]. Future development of agile SAR antennas and innovative acquisi-
 222 tion modes, such as Bi-Directional SAR or SuperSAR, should provide two simultaneous
 223 squinted views with continuous spatial sampling [*Mittermayer et al.*, 2013; *Jung et al.*,
 224 2015], thereby truly extending the InSAR technique towards full 3D capability.

Appendix A: Along-track ground displacement from TOPS interferometry

A1. Principle of “burst overlap interferometry”

In along-track double-difference interferograms, the azimuth displacement Δx_{az} is proportional to the azimuth time shift induced by target displacement along the azimuth time axis Δt_{az} (or equally the azimuth misregistration) and to the difference in instantaneous Doppler frequency Δf_{ovl} between forward and backward view in the overlap region [*Scheiber and Moreira*, 2000]:

$$\Delta\Phi_{ovl} = 2\pi\Delta f_{ovl}\Delta t_{az} = 2\pi\Delta f_{ovl}\frac{\Delta x_{az}}{\Delta x_s}\Delta t_s \quad (\text{A1})$$

where Δt_s is the azimuth sampling and Δx_s is the azimuth pixel size. In TOPS wide-swath mode, the frequency difference Δf_{ovl} is the product of the effective Doppler rate K_t and the duration of a full TOPS cycle T_{cycle} [Prats-Iraola et al., 2012]:

$$\Delta f_{\text{ovl}} = |K_t| T_{\text{cycle}} \quad (\text{A2})$$

The effective Doppler rate K_t results from the combination of the classical Doppler rate induced by platform motion K_a and the supplemental effect K_s induced by beam steering at a rate k_Ψ from the aft to the fore [De Zan and Guarnieri, 2006]:

$$K_t = \frac{K_a K_s}{K_a - K_s} \quad ; \quad K_a = -\frac{2v_s^2}{\lambda R_o} \quad ; \quad K_s \approx \frac{2v_s}{\lambda} k_\Psi \quad (\text{A3})$$

The same result can be deduced equivalently by considering the difference between line-of-sight (LOS) vectors for the two observation directions available in burst overlaps. The azimuth displacement is the projection of ground motion \vec{u}_{displ} onto the difference, within the overlap region, between the LOS vectors \vec{k}_{fw} and \vec{k}_{bw} of the forward interferogram and the backward interferogram, respectively (Figure 1b) :

$$\begin{aligned} \Delta \Phi_{\text{ovl}} = (\Delta \Phi_{\text{fw}} - \Delta \Phi_{\text{bw}}) &= \frac{4\pi}{\lambda} \vec{u}_{\text{displ}} \cdot (\vec{k}_{\text{fw}} - \vec{k}_{\text{bw}}) \\ &= \frac{4\pi}{\lambda} \Delta x_{\text{az}} \cdot \|\vec{j}_{\text{diff}}\| \end{aligned} \quad (\text{A4})$$

$$\text{with} \quad : \quad \vec{j}_{\text{diff}} = \vec{k}_{\text{fw}} - \vec{k}_{\text{bw}} \approx \Delta \Psi_{\text{ovl}} \cdot \vec{j}_{\text{along-track}} \quad (\text{A5})$$

where $\vec{j}_{\text{along-track}}$ is a horizontal unit vector parallel to the satellite track. In TOPS mode, the squint angle difference $\Delta \Psi_{\text{ovl}}$ between two consecutive overlaps for a given sub-swath can be deduced from the beam steering rate k_Ψ and the time separation between overlaps $\Delta \eta_{\text{ovl}}$:

$$\Delta \Psi_{\text{ovl}} = \Delta \eta_{\text{ovl}} k_\Psi \quad (\text{A6})$$

225 Typical numerical values of the above parameters for Sentinel-1 TOPS IW mode are pro-
 226 vided in Table A1. Ultimately, the along-track displacement Δx_{az} (in cm) is obtained by
 227 multiplying the double-difference phase $\Delta\Phi_{ovl}$ (in radian) by a factor $\sim 21 - 25$ cm/rad,
 228 meaning that a full along-track fringe represents an along-track displacement of ~ 130 cm
 229 (for comparison, the radian-to-cm conversion factor equals ~ 0.44 cm/rad for the ~ 2.8 cm
 230 across-track fringe).

A2. Uncertainty assessment

From a signal processing point-of-view, the theoretical accuracy achieved by the double-difference interferogram in burst overlaps is given by the error standard deviation [Bamler and Eineder, 2005; Prats-Iraola et al., 2012] :

$$\sigma_{ovl} = \frac{1}{2\pi\Delta f_{ovl}} \frac{1}{\sqrt{N}} \frac{\sqrt{1-\gamma^2}}{\gamma} \frac{1}{\Delta t_s}, \quad (\text{A7})$$

here provided in units of resolution elements. In this expression, N is the number of pixels used in the spatial averaging, γ is the coherence and Δf_{ovl} is the spectral separation in the overlap region (~ 4 kHz for Sentinel IW). As shown in Figure A1, the expected accuracy strongly depends on the number of independent pixels used in the averaging, but less so on the coherence. In case of a uniform shift across the whole burst overlap region (i.e. no deformation), N may exceed a million pixels, so that an accuracy better than 0.1 cm can be reached. However, the accuracy decreases to 0.3–1 cm if displacement changes over distances of the order of 1 km, and up to 10 cm for 100 m posting in adverse coherence conditions. These estimates are in rough agreement with the residual fit to the GPS measured for the Illapel earthquake data set (RMS=3–5 cm, Section 3.2), which corresponds to relatively good coherence conditions ($\gamma > 0.5$). For comparison, the standard devia-

tions from Coherent cross-correlation (CCC) [*Bamler and Eineder, 2005; De Zan, 2011*] and Incoherent (amplitude) cross-correlation (ICC) [*De Zan, 2014*] are, respectively :

$$\sigma_{ICC} = \sqrt{\frac{3}{2N} \frac{\sqrt{1-\gamma^2}}{\pi\gamma}} \quad ; \quad \sigma_{CCC} = \sqrt{\frac{3}{10N} \frac{\sqrt{2+5\gamma^2-7\gamma^4}}{\pi\gamma^2}} \quad (\text{A8})$$

231 For a given number of averaged pixels, the performance of the present method is better,
232 by one order of magnitude, than that of ICC and CCC (Figure A1).

233 From a practical point of view, the double-difference along-track phase is not contami-
234 nated by atmospheric phase screen, which is the main source of error for multi-temporal
235 InSAR [e.g. *Zebker et al., 1997; Hanssen, 2001*]. Nevertheless, along-track InSAR being
236 a relative measurement, it can be affected by long-spatial-wavelength nuisance stemming
237 from residual large-scale misregistration due to geometric approximations and/or orbit er-
238 rors. This effect translates locally into a bias that may reach several centimeters. This bias
239 can be mitigated by adjustment of a planar or higher order polynomial trend in distant
240 regions unaffected by the tectonic signal, or accounted for as an unknown during source
241 modeling. Alternatively, external data, such as GPS, can be used to provide a reference.
242 Interpolation between burst overlaps can also lead to aliasing of the displacement field.
243 The induced errors depend on the smallest spatial wavelength of the deformation. In par-
244 ticular, a complex displacement field (e.g. induced by shallow faulting) will significantly
245 jeopardize the validity of the interpolation.

246 **Acknowledgments.**

247 The Sentinel-1 data used for this study are provided by ESA / Copernicus. Interfero-
248 metric processing was carried out using a modified version of ROIPAC software [*Rosen*
249 *et al., 2004*]. Most figures were designed and some processing steps (filtering, interpola-

tion) were performed with help of GMT software [Wessel and Smith, 1991]. The GPS
observations used in this study were acquired through the Centro Sismológico Nacional
(CSN) and the French–Chilean Laboratoire International Associé (LIA) geodetic net-
works. This project was supported by PNTS grant number “PNTS-2015-09” and by the
“MEGACHILE” project funded by the Agence Nationale de la Recherche (ANR). This is
IPGP contribution number 3721.

References

- Bamler, R., and M. Eineder (2005), Accuracy of differential shift estimation by correlation
and split-bandwidth interferometry for wideband and delta-k sar systems, *Geoscience
and Remote Sensing Letters, IEEE*, 2(2), 151–155.
- Barbot, S., Y. Hamiel, and Y. Fialko (2008), Space geodetic investigation of the coseismic
and postseismic deformation due to the 2003 Mw7. 2 Altai earthquake: Implications
for the local lithospheric rheology, *Journal of Geophysical Research: Solid Earth (1978–
2012)*, 113(B3).
- Bechor, N. B., and H. A. Zebker (2006), Measuring two-dimensional movements using a
single InSAR pair, *Geophysical research letters*, 33(16).
- De Zan, F. (2011), Coherent shift estimation for stacks of sar images, *Geoscience and
Remote Sensing Letters, IEEE*, 8(6), 1095–1099.
- De Zan, F. (2014), Accuracy of incoherent speckle tracking for circular gaussian signals,
IEEE Geoscience and Remote Sensing Letters, 11(1), 264–267.
- De Zan, F., and A. M. Guarnieri (2006), TOPSAR: Terrain observation by progressive
scans, *Geoscience and Remote Sensing, IEEE Transactions on*, 44(9), 2352–2360.

- 271 De Zan, F., P. Prats-Iraola, R. Scheiber, and A. Rucci (2014), Interferometry with tops:
272 coregistration and azimuth shifts, in *EUSAR 2014; 10th European Conference on Syn-*
273 *thetic Aperture Radar; Proceedings of*, pp. 1–4, VDE.
- 274 De Zan, F., P. Prats-Iraola, and M. Rodriguez-Cassola (2015), On the dependence of
275 delta-k efficiency on multilooking, *Geoscience and Remote Sensing Letters, IEEE*, *12*(8),
276 1745–1749.
- 277 Ducret, G. (2013), Mesure de déformation par interférométrie radar : développements
278 méthodologiques et applications à la subduction chilienne., Ph.D. thesis, Institut de
279 Physique du Globe de Paris, France.
- 280 Fialko, Y., M. Simons, and D. Agnew (2001), The complete (3-D) surface displace-
281 ment field in the epicentral area of the 1999 M_w 7.1 Hector Mine earthquake, Cali-
282 fornia, from space geodetic observations, *Geophys. Res. Lett.*, *28*(16), 3063–3066, doi:
283 10.1029/2001GL013174.
- 284 Goldstein, R. M., H. A. Zebker, and C. L. Werner (1988), Satellite radar interferometry-
285 two-dimensional phase unwrapping, *Radio science*, *23*(4), 713–720.
- 286 González, P. J., M. Bagnardi, A. J. Hooper, Y. Larsen, P. Marinkovic, S. V. Samsonov,
287 and T. J. Wright (2015), The 2014–2015 eruption of Fogo volcano: Geodetic modeling
288 of Sentinel-1 TOPS interferometry, *Geophysical Research Letters*, *42*(21), 9239–9246.
- 289 Grandin, R. (2015), Interferometric Processing of SLC Sentinel-1 TOPS Data, in *Proceed-*
290 *ings of the 2015 ESA Fringe workshop, ESA Special Publication, SP*, vol. 731.
- 291 Grandin, R., A. Socquet, R. Binet, Y. Klinger, E. Jacques, J.-B. de Chabalier, G. King,
292 C. Lasserre, S. Tait, P. Tapponnier, et al. (2009), September 2005 Manda Hararo-

- 293 Dabbahu rifting event, Afar (Ethiopia): constraints provided by geodetic data, *Journal*
294 *of Geophysical Research: Solid Earth (1978–2012)*, 114(B8).
- 295 Grandin, R., M. Vallée, C. Satriano, R. Lacassin, Y. Klinger, M. Simoes, and L. Bollinger
296 (2015), Rupture process of the mw= 7.9 2015 gorkha earthquake (nepal): insights into
297 himalayan megathrust segmentation, *Geophysical Research Letters*, 42(20), 8373–8382.
- 298 Hanssen, R. F. (2001), *Radar interferometry: data interpretation and error analysis*,
299 vol. 2, Springer Science & Business Media.
- 300 Holzner, J., and R. Bamler (2002), Burst-mode and scansar interferometry, *Geoscience*
301 *and Remote Sensing, IEEE Transactions on*, 40(9), 1917–1934.
- 302 Jung, H.-S., J.-S. Won, and S.-W. Kim (2009), An improvement of the performance of
303 multiple-aperture SAR interferometry (MAI), *Geoscience and Remote Sensing, IEEE*
304 *Transactions on*, 47(8), 2859–2869.
- 305 Jung, H.-S., W.-J. Lee, and L. Zhang (2014), Theoretical Accuracy of Along-Track
306 Displacement Measurements from Multiple-Aperture Interferometry (MAI), *Sensors*,
307 14(9), 17,703–17,724.
- 308 Jung, H.-S., Z. Lu, A. Shepherd, and T. Wright (2015), Simulation of the supersar multi-
309 azimuth synthetic aperture radar imaging system for precise measurement of three-
310 dimensional earth surface displacement, *Geoscience and Remote Sensing, IEEE Trans-*
311 *actions on*, 53(11), 6196–6206.
- 312 Melgar, D., W. Fan, S. Riquelme, J. Geng, L. Liang, M. Fuentes, G. Vargas, R. Allen,
313 P. Shearer, and E. Fielding (2016), Slip segmentation and slow rupture to the trench
314 during the 2015, Mw8.3 Illapel, Chile earthquake, *Geophys. Res. Lett.*

- 315 Meta, A., P. Prats, U. Steinbrecher, J. Mittermayer, and R. Scheiber (2008), TerraSAR-X
316 TOPSAR and ScanSAR comparison, in *Synthetic Aperture Radar (EUSAR), 2008 7th*
317 *European Conference on*, pp. 1–4, VDE.
- 318 Michel, R., J.-P. Avouac, and J. Taboury (1999), Measuring ground displacements from
319 SAR amplitude images: application to the landers earthquake, *Geophys. Res. Lett.*, *26*,
320 875–878, doi:10.1029/1999GL900138.
- 321 Mittermayer, J., S. Wollstadt, P. Prats-Iraola, P. López-Dekker, G. Krieger, and A. Mor-
322 eira (2013), Bidirectional sar imaging mode, *Geoscience and Remote Sensing, IEEE*
323 *Transactions on*, *51*(1), 601–614.
- 324 Peltzer, G., F. Crampé, and G. King (1999), Evidence of nonlinear elasticity of the crust
325 from the Mw7. 6 Manyi (Tibet) earthquake, *Science*, *286*(5438), 272–276.
- 326 Prats-Iraola, P., R. Scheiber, L. Marotti, S. Wollstadt, and A. Reigber (2012), TOPS
327 interferometry with TerraSAR-X, *Geoscience and Remote Sensing, IEEE Transactions*
328 *on*, *50*(8), 3179–3188.
- 329 Pritchard, M., C. Ji, and M. Simons (2006), Distribution of slip from 11 mw \geq 6 earthquakes
330 in the northern chile subduction zone, *Journal of Geophysical Research: Solid Earth*
331 *(1978–2012)*, *111*(B10).
- 332 Rosen, P. A., S. Henley, G. Peltzer, and M. Simons (2004), Updated Repeat Orbit Interfer-
333 ometry Package Released, *Eos Trans. AGU*, *85*(5), 47–47, doi:10.1029/2004EO050004.
- 334 Ruiz, S., E. Klein, E. Rivera, P. Poli, M. Métois, C. Vigny, J. C. Baez, G. Vargas, F. Ley-
335 ton, R. Madariaga, and L. Fleitout (2016), The seismic sequence of the 16 September
336 2005, Illapel Mw 8.3 earthquake, *Seismological Research Letters*, *under review*.

- 337 Scheiber, R., and A. Moreira (2000), Coregistration of interferometric sar images using
338 spectral diversity, *Geoscience and Remote Sensing, IEEE Transactions on*, 38(5), 2179–
339 2191.
- 340 Scheiber, R., M. Jager, P. Prats-Iraola, F. De Zan, and D. Geudtner (2015), Speckle Track-
341 ing and Interferometric Processing of TerraSAR-X TOPS Data for Mapping Nonsta-
342 tionary Scenarios, *Selected Topics in Applied Earth Observations and Remote Sensing*,
343 *IEEE Journal of*, 8(4), 1709–1720.
- 344 Simons, M., and P. Rosen (2007), Interferometric synthetic aperture radar geodesy, *Trea-*
345 *tise on Geophysics*, 3, 391–446.
- 346 Torres, R., P. Snoeij, D. Geudtner, D. Bibby, M. Davidson, E. Attema, P. Potin, B. Rom-
347 men, N. Floury, M. Brown, et al. (2012), Gmes sentinel-1 mission, *Remote Sensing of*
348 *Environment*, 120, 9–24.
- 349 Wessel, P., and W. H. F. Smith (1991), Free software helps map and display data, *EOS*
350 *Transactions*, 72, 441–441, doi:10.1029/90EO00319.
- 351 Wright, T. J., B. E. Parsons, and Z. Lu (2004), Toward mapping surface defor-
352 mation in three dimensions using InSAR, *Geophys. Res. Lett.*, 31(1), 1607, doi:
353 10.1029/2003GL018827.
- 354 Zebker, H. A., P. A. Rosen, and S. Hensley (1997), Atmospheric effects in interferometric
355 synthetic aperture radar surface deformation and topographic maps, *Journal of Geo-*
356 *physical Research: Solid Earth (1978–2012)*, 102(B4), 7547–7563.

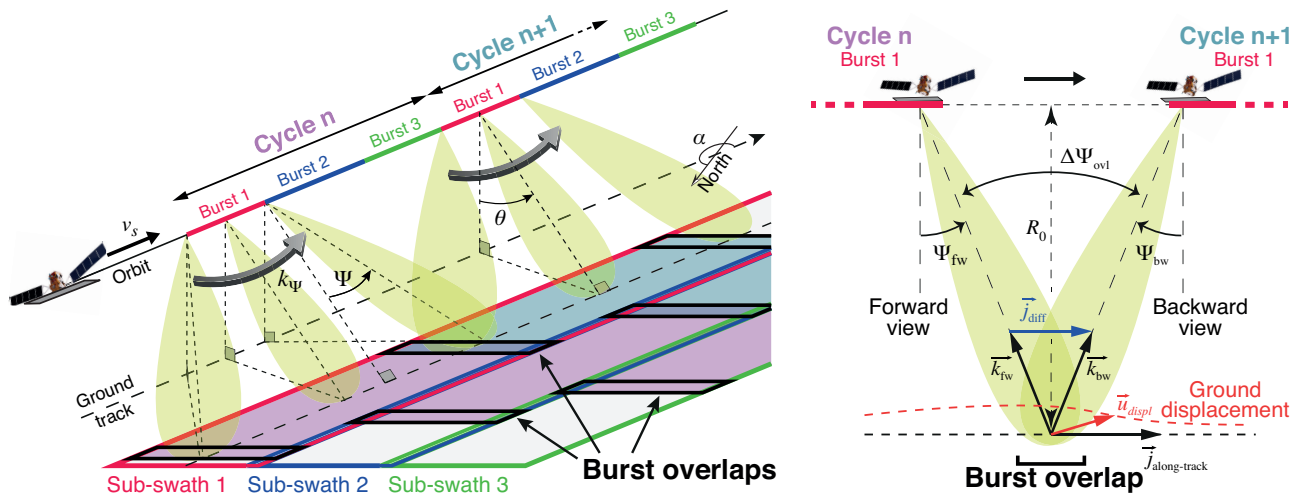


Figure 1. Left: principle of TOPS imaging mode. Right: squint angle diversity in burst overlap regions.

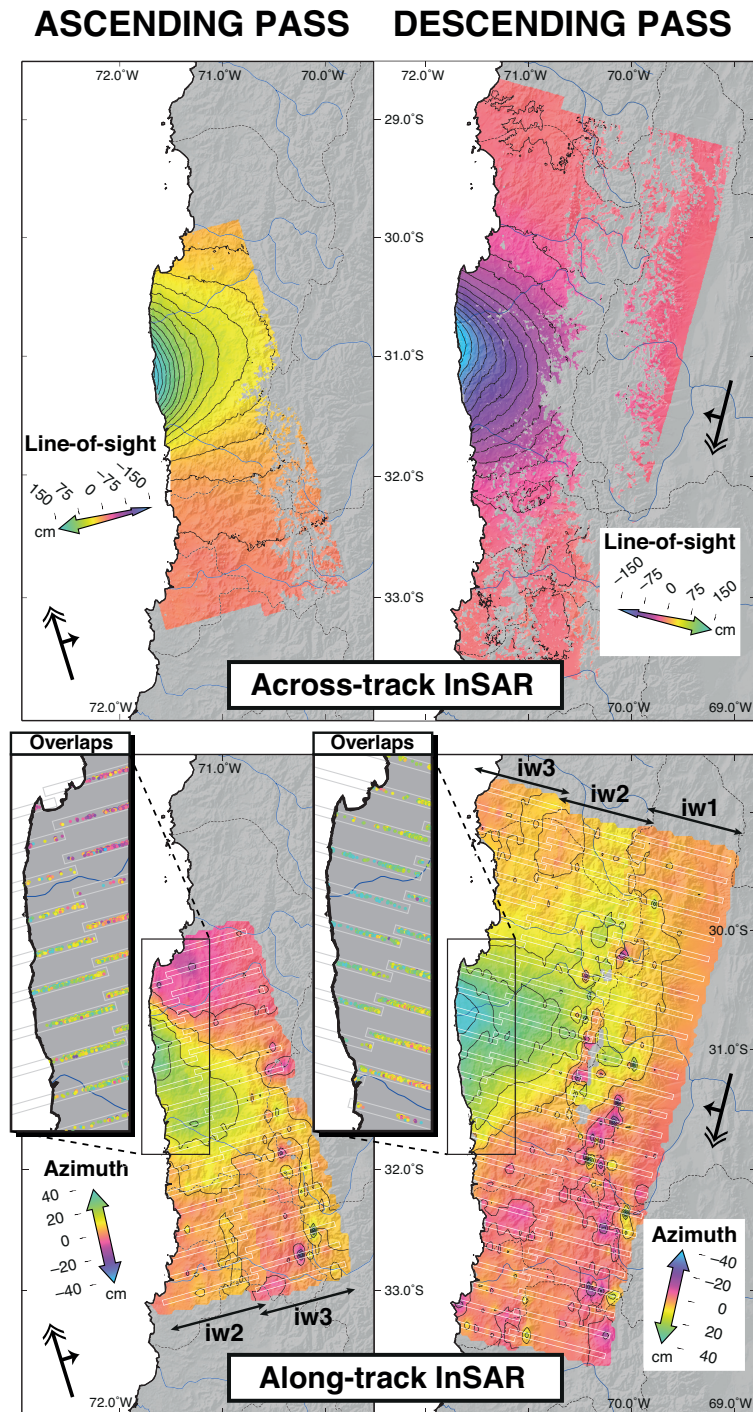


Figure 2. Across-track (top) and along-track (bottom) displacement field from Sentinel-1 InSAR. Note the different color scaling for across-track and along-track InSAR. The left and right panels correspond to ascending and descending passes, respectively. Double headed arrow shows direction of flight of the platform. White rectangles in bottom panels indicate regions of burst overlaps. The along-track displacement field was filtered and interpolated between regions

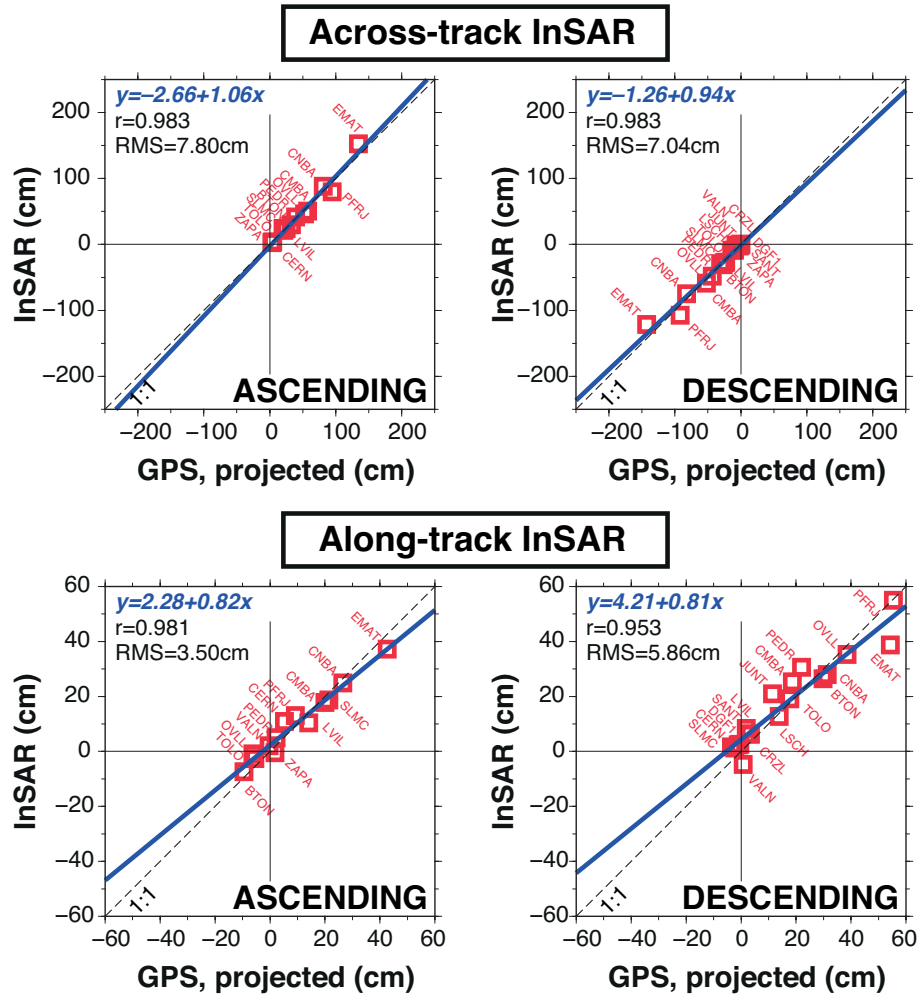


Figure 3. Linear regression between GPS and (top) across-track InSAR or (bottom) along-track InSAR. Left panels are for the ascending pass, right panels for the descending pass (same ordering as in Figure 2). Note the different scaling for across-track and along-track InSAR.

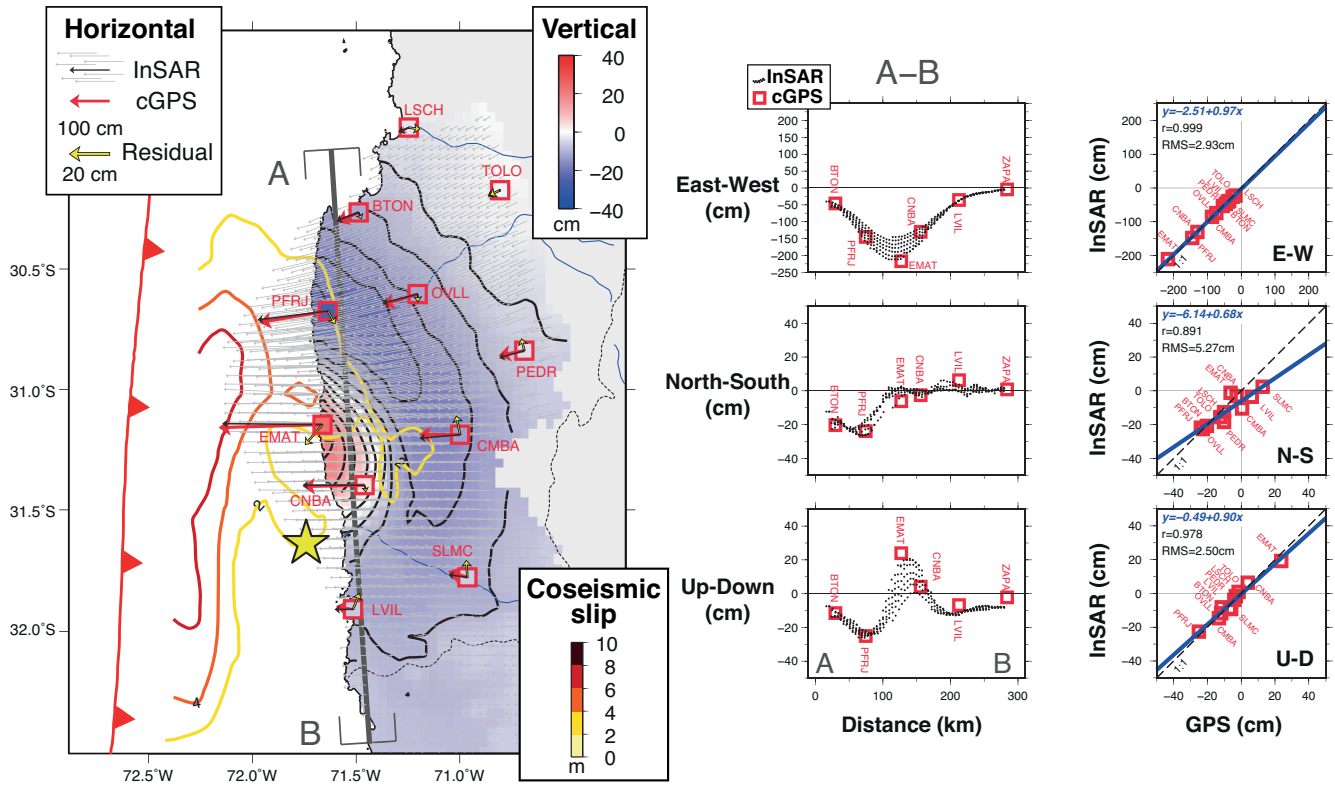


Figure 4. Left: 3D surface displacement reconstructed from Sentinel-1 InSAR. Red arrows show displacement at continuous GPS sites (cGPS), while color fill in red squares interior represents the vertical component of displacement from GPS [Ruiz et al., 2016]. Black arrows show displacement deduced from Sentinel-1 InSAR at locations of GPS benchmarks. Residuals are shown in yellow, with enhanced scaling. Grey arrows show horizontal displacement sampled on a regular grid. The colored grid in the background shows the vertical component of displacement on the same regular grid, with contours at 5 cm interval overlaid. Coseismic slip contours from USGS are shown for comparison (http://earthquake.usgs.gov/earthquakes/eventpage/us20003k7a#scientific_fault). Center: transect showing comparison between Sentinel-1 InSAR and GPS. Location of the profile is shown in left panel. Top row: east-west component; middle row: north-south component; bottom row: vertical component. Sign convention is right-handed ENU. Note the different scaling for the east-west component. Right: linear regression between Sentinel-1 InSAR and GPS displacements at GPS sites.

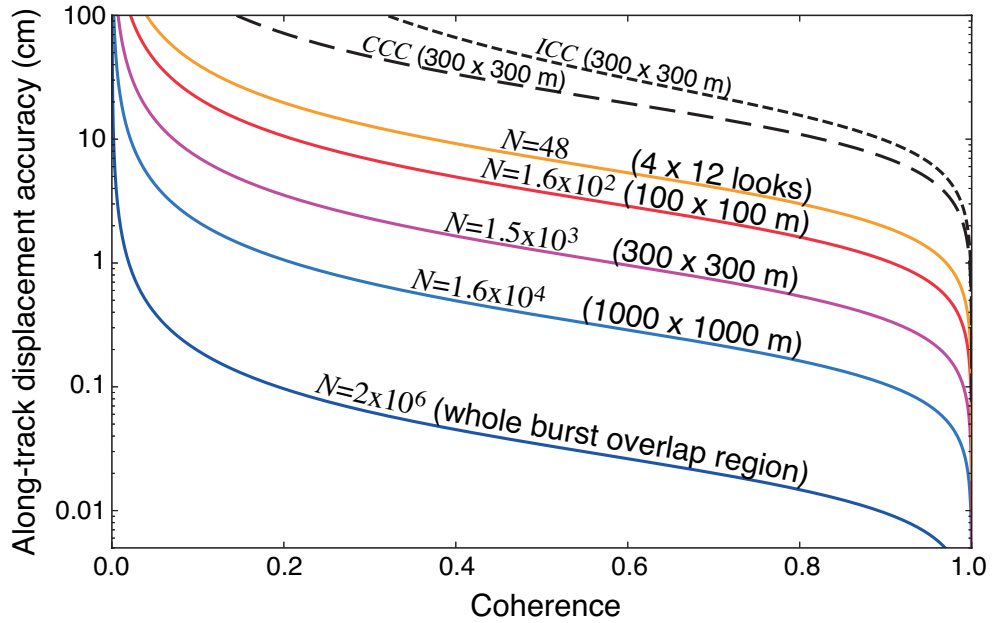


Figure A1. Theoretical accuracy of the along-track displacement achieved by Sentinel-1 burst-overlap interferometry, as a function of coherence γ , for an azimuth pixel size $\Delta x_s = 14$ m (color lines, Equation A7). Several cases are distinguished, depending on the number of full-resolution pixels N used for the averaging. The accuracy of coherent and incoherent cross-correlation techniques (respectively CCC and ICC) at 300×300 m posting is shown for comparison (black dashed lines, Equation A8).

Table A1. Parameters of Sentinel-1 IW data used in this study (descending pair)

| Parameter | | 1 | 2 | 3 |
|---|--------------------|--------------------------|--------------------------|--------------------------|
| Sub-swath | | | | |
| Range ^a | R_o | 829 km | 879 km | 933 km |
| Incidence angle ^a | θ | 34° | 39° | 44° |
| Antenna steering rate | k_Ψ | 1.59 deg.s ⁻¹ | 0.98 deg.s ⁻¹ | 1.40 deg.s ⁻¹ |
| Time separation between overlaps | $\Delta\eta_{ovl}$ | 0.80 s | 0.96 s | 0.82 s |
| Squint difference in overlap region | $\Delta\Psi_{ovl}$ | 1.28° | 0.94° | 1.15° |
| Doppler rate due to platform motion ^a | K_a | -2260 Hz | -2131 Hz | -2008 Hz |
| Doppler rate due to antenna steering ^a | K_s | 7593 Hz | 4679 Hz | 6672 Hz |
| Doppler rate in focused SLC ^a | K_t | 1742 Hz | 1464 Hz | 1544 Hz |
| Wavelength | λ | | 5.55 cm | |
| Platform heading (clockwise w.r.t. north) | α | | -167.2° | |
| Platform velocity | v_S | | 7211 m.s ⁻¹ | |
| Azimuth sampling | Δt_s | | 0.002056 s | |
| Azimuth pixel size | Δx_s | | 14.07 m | |
| Burst cycle duration | T_{cycle} | | 2.75 s | |

^a At mid-range